Nanoscale

Near-Infrared Emitting Dual-Stimuli-Responsive Carbon Dots from Endogenous Bile Pigments

Journal:	*Nanoscale*
Manuscript ID	NR-ART-02-2021-001295.R1
Article Type:	Paper
Date Submitted by the Author:	25-Jun-2021
Complete List of Authors:	Fathi, Parinaz; University of Illinois at Urbana-Champaign, Bioengineering Moitra, Parikshit; University of Illinois at Urbana-Champaign, Bioengineering McDonald, Madeleine M. ; University of Illinois at Urbana-Champaign, Bioengineering Esch, Mandy; NIST, Pan, Dipanjan; UMBC, CHemical, Biochemical and Environmental Engineering; UMB,

ARTICLE

Near-Infrared Emitting Dual-Stimuli-Responsive Carbon Dots from Endogenous Bile Pigments

Received 00th January 20xx,
Accepted 00th January 20xx

DOI: 10.1039/x0xx00000x

Parinaz Fathi,[a,b] Parikshit Moitra,[c] Madeleine M. McDonald,[a,b] Mandy B. Esch,[d] Dipanjan Pan[a,b,e,f]*

Carbon dots are biocompatible nanoparticles suitable for a variety of biomedical applications. Careful selection of carbon dot precursors and surface modification techniques has allowed for the development of carbon dots with strong near-infrared fluorescence emission. However, carbon dots that provide strong fluorescence contrast would prove even more useful if they were also responsive to stimuli. In this work, endogenous bile pigments bilirubin (BR) and biliverdin (BV) were used for the first time to synthesize stimuli-responsive carbon dots (BR-CDots and BV-CDots respectively). The precursor choice lends these carbon dots with spectroscopic characteristics that are enzyme-responsive and pH-responsive without the need for surface modifications post-synthesis. Both BV- and BR-CDots are water-dispersible and provide fluorescence contrast, while retaining the stimuli-responsive behaviors intrinsic to their precursors. Nanoparticle Tracking Analysis revealed that the hydrodynamic size of the BR-CDots and BV-CDots decreased with exposure to bilirubin oxidase and biliverdin reductase, respectively, indicating potential enzyme-responsive degradation of the carbon dots. Fluorescence spectroscopic data demonstrate that both BR-CDots and BV-CDots exhibit changes in their fluorescence spectra in response to changes in pH, indicating that these carbon dots have potential applications in pH sensing. In addition, BR-CDots are biocompatible and provide near-infrared fluorescence emission when excited with light at wavelengths of 600 nm or higher. This work demonstrates the use of rationally selected carbon sources for obtaining near-infrared fluorescence and stimuli-responsive behavior in carbon dots that also provide strong fluorescence contrast.

Introduction

Optical imaging with near-infrared wavelengths provides strong signals with minimal interference from tissue autofluorescence.[1] Carbon nanoparticles or carbon dots are a promising platform for near-infrared fluorescence imaging due to their relatively simple synthesis procedure, stable fluorescence that can be advantageous in studying naturally-occurring phytochromes, and known biocompatibility. Rational selection of precursors and reaction conditions has yielded carbon nanoparticles with high quantum yield,[2–4] high near-infrared emission,[5–8] and stimuli-responsive behavior[9,10], for *in vitro*, *in vivo*, and fundamental applications[11–18]. Despite these advantages, there have been few reports of tetrapyrrolic precursors for carbon dot synthesis and the effects of the use of these precursors on carbon dot behavior.[19–23] Only recently, the use of nanoparticles made of bilirubin, a naturally-occurring fluorescent tetrapyrrolic pigment, has been reported.[24–29] The use of such pigments as nanoparticle precursors generates nanoparticles that provide contrast for biological imaging. Despite this observation, the use of bilirubin as a precursor for nanoparticles can prove challenging due to its limited solubility in water.[24,28] In this work, we sought to utilize tetrapyrrolic bilirubin and biliverdin, endogenous tetrapyrrole molecules found in bile, as carbon dot precursors to generate strong near-infrared fluorescence contrast and to exploit their stimuli-responsive behaviors.

[a] *Departments of Bioengineering, Materials Science and Engineering, and Beckman Institute, University of Illinois 61801, United States*
[b] *Mills Breast Cancer Institute, Carle Foundation Hospital, Urbana, Illinois 61801, United States*
[c] *Department of Pediatrics, University of Maryland School of Medicine, Baltimore, MD 21201, U.S.*
[d] *Biomedical Technologies Group, Microsystems and Nanotechnology Division, Physical Measurement Laboratory, National Institute of Standards and Technology, Gaithersburg, Maryland 20899, United States*
[e] *Departments of Diagnostic Radiology and Nuclear Medicine and Pediatrics, University of Maryland Baltimore, Health Sciences Facility III, 670 W Baltimore St., Baltimore, Maryland, 21201, United States*
[f] *Department of Chemical, Biochemical and Environmental Engineering, University of Maryland Baltimore County, Interdisciplinary Health Sciences Facility, 1000 Hilltop Circle Baltimore, Maryland, 21250, United StatesAddress here.*
** Email: dipanjan@som.umaryland.edu*
Electronic Supplementary Information (ESI) available: TEM images, IVIS tissue phantom images, IVIS ROI analysis, particle stability experiments, fluorescence microscopy images, fluorescence spectra, and FTIR spectra. See DOI: 10.1039/x0xx00000x

Biliverdin, a green phytochrome, is the end product of a reaction between heme and heme oxygenase, which is further reduced into the yellow phytochrome bilirubin through the action of an enzyme, biliverdin reductase.[30] Bilirubin can be re-converted to biliverdin through the action of bilirubin oxidase,[31,32] or in response to ultraviolet (UV) irradiation.[33] Biliverdin and bilirubin can be distinguished from each other by biliverdin's high near-infrared absorbance peak at ca. 670 nm[34,35] and bilirubin's near-infrared fluorescence emission[36–39] respectively. Biliverdin and bilirubin are also known to be pH-sensitive,[33] and the use of other pyrrolic molecules for fluorometric pH sensing has been reported.[40,41] Here we present the synthesis and characterization of carbon nanoparticles derived from biliverdin and bilirubin. We utilized these two bile pigments as precursors for carbon nanoparticle synthesis to exploit their inherent fluorescence properties and to utilize external stimuli to alter the particle behaviors **(Scheme 1)**.

Using a solvothermal synthesis, we created water-dispersible carbon dots from bilirubin and biliverdin. The resulting carbon dots retained many of the properties of their precursors, including their ability to respond to enzymatic exposure or changes in pH. To the best of our knowledge, ours is the first demonstration of a carbon dot nanoparticle-based-system with precursor-derived alterable photophysical properties that can be stimulated by an external trigger. Additionally, we found that the bilirubin-derived carbon dots had high biocompatibility and provided strong contrast in *ex vivo* tissue-imaging experiments.

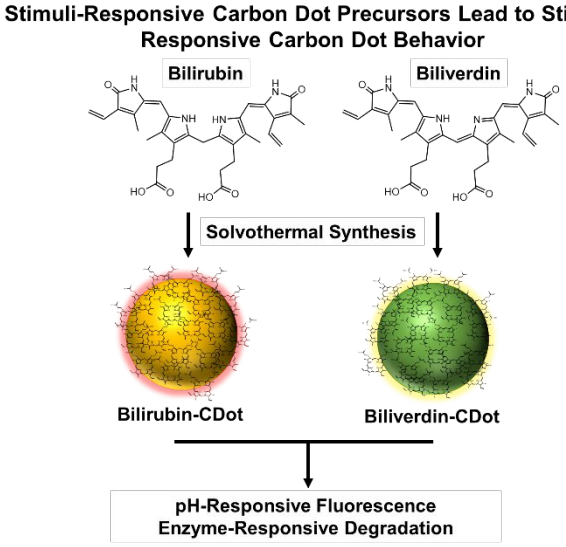

Scheme 1. Schematic representation of stimuli-responsive CDots. Carbon dots derived from bilirubin and biliverdin possess photophysical behaviors that can be altered in response to exposure to different pH values. The BR-CDots and BV-CDots also exhibit a decrease in size after exposure to bilirubin oxidase and biliverdin reductase, respectively.

Results and Discussion

Carbon Dot Synthesis and Characterization

BR-CDots and BV-CDots were synthesized through solvothermal synthesis with precursor concentrations of 0.17 mol/L in a mixture of dimethylsulfoxide (DMSO) and water as co-solvents. Particles were filtered, then subjected to rotary evaporation and lyophilization, followed by resuspension at equivalent mass concentrations in water. Detailed experimental methods are described in the experimental section.

Carbon dot formation was confirmed with TEM imaging **(Figure S1)**. These images reveal that the anhydrous size of the BV-CDots is smaller than the anhydrous size of the BR-CDots. High-resolution TEM imaging of BR-CDots revealed lattice fringes that are characteristic of previously reported carbon dots **(Figure 1A)**.[42–45] Lattice fringes measured at two different locations within the BR-CDot had an average d-spacing of 0.3087 ± 0.0537 nm and 0.3266 ± 0.0658 nm. These values are in agreement with accepted d-spacing values for graphitic structures.[46,47] This confirms that the particles described in this work are carbon dots that are composed of graphitic carbon. The exclusion of unreacted bilirubin and biliverdin from the carbon dot suspensions was confirmed with mass spectrometry **(Figure 1B)**, specifically by the absence of the mass spectrometry peaks that would be expected for bilirubin and biliverdin. The absence of mass spectrometry peaks at m/z values of 584.66 (bilirubin), 585.67 (bilirubin + H^+), 602.69 (bilirubin + NH_4^+), 607.65 (bilirubin + Na^+), 617.69 (bilirubin + CH_3OH + H^+), 623.62 (bilirubin + K^+), 626.69 (bilirubin + ACN + H^+), and 629.63 (bilirubin + 2 Na^+ - H^+) in BR-CDots, and 582.65 (biliverdin), 583.65 (biliverdin + H^+), 600.68 (biliverdin + NH_4^+), 605.64 (biliverdin + Na^+), 615.68 (biliverdin + CH_3OH + H^+), 621.61 (biliverdin + K^+), 624.68 (biliverdin + ACN + H^+), and 627.62 (biliverdin + 2 Na^+ - H^+) in BV-CDots confirmed the removal of any excess molecular bilirubin and biliverdin during the nanoparticle synthesis and purification process. This confirms that the fluorescence behavior observed in this work comes from the particles themselves rather than any leftover bilirubin or biliverdin.

To complement the conclusions drawn from mass spectrometry and high-resolution TEM imaging, we conducted Fourier transform infrared spectroscopy (FT-IR) experiments **(Figure S2)**. These experiments demonstrated that BR-CDots and BV-CDots retained some of the peaks from their respective precursors, indicating that some imidolic structures were likely retained by the carbon dots. Bilirubin's poor solubility in water,[48,49] coupled with the high BR-CDot water solubility and the mass spectroscopic data discussed above, confirm that the carbon dot suspensions were not contaminated by unreacted precursors and that the carbon dots were not simply surface-functionalized with the tetrapyrrolic molecules. If BR-CDots were composed of a graphitic core and simply coated in pure bilirubin, their suspension in water would have likely proved challenging. Furthermore, the pure bilirubin and biliverdin would have been identified in the mass spectra.

We further conducted X-ray photoelectron spectroscopy (XPS) **(Figure 1C)** to elucidate the elemental composition of the surface of these particles**.** BR-CDots and BV-CDots retained C 1s, N 1s, and O 1s atoms from their precursors **(Figure 1C i)**. The spectra for BR-CDots and BV-CDots appear quite similar due to the inherent similarities between bilirubin and biliverdin, the carbon dot precursors. In addition to identifying the presence of atoms that were within the precursor structures, we also identified the presence of S 2p, likely caused by the incorporation of sulfur atoms from DMSO during the solvothermal synthesis process. The CDots were found to be primarily composed of C 1s and O 1s **(Figure 1C ii)**. Deconvolution of the C 1s peak revealed the presence of characteristic energies corresponding to the presence of carbon atoms in C-C/C=C, C-N/C-O,

and COOH configurations **(Figure 1C iii)**. These findings serve to further confirm that the synthesized carbon dots successfully retained atoms from their precursor molecules despite not retaining the whole tetrapyrrolic molecules.

Evaluation of Photophysical Properties and Stimuli Responsive Behaviors

an excitation wavelength of 365 nm the BR-CDots have red-shifted fluorescence emission compared to the BV-CDots **(Figure 2C)**.

Carbon dot stimuli responsive behavior was explored by exposing them to enzymes or various pH conditions. To explore enzyme-responsiveness, the pH of the solution containing the CDots was raised to 8~9 in order to enable enzyme activity, and particles were then exposed to enzymes (with cofactors). We reasoned that

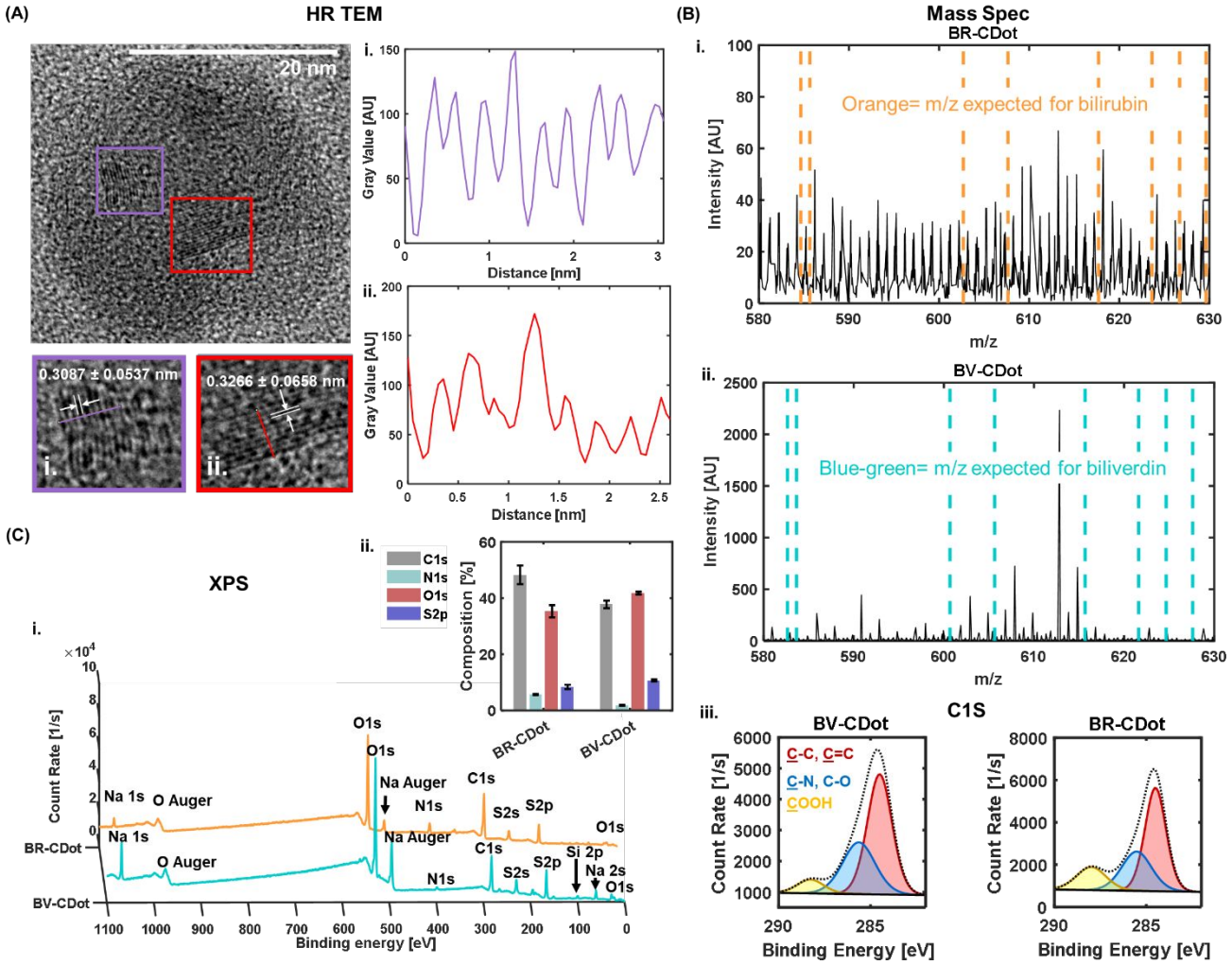

Figure 1. Characterization of bile pigment-derived CDots. **(A)** High-resolution TEM image of a BR-CDot, demonstrating the presence of lattice fringes. Lattice fringe quantification was done using profile plots for purple inset **(i)** and blue inset **(ii)**. This confirms that the nanoparticles studied in this work are carbon dots that contain graphitic carbon. **(B)** Mass spectroscopy of BR-CDots **(i)** and BV-CDots **(ii)**. Orange and green dashed lines represent expected m/z locations for bilirubin (or bilirubin + ions) and biliverdin (or biliverdin + ions), respectively. The absence of peaks at the m/z values identified by the dashed lines confirm that the carbon dot suspension does not contain any unreacted tetrapyrrolic precursor. **(C)** X-ray photoelectron spectroscopy studies. **(i)** XPS spectra of BR-CDots and BV-CDots. Peaks associated with Si result from the substrate (gold-coated silicon). **(ii)** XPS % composition analysis of C 1s, N 1s, O 1s, and S 2p atoms. The abundant presence of C 1s and O 1s atoms aligns with expectations based on bilirubin and biliverdin structures, as well as with typical carbon dot compositions. **(iii)** Deconvolved C 1s XPS peaks. Deconvolution reveals the presence of C 1s atoms corresponding to C-C/C=C, C-N/C-O, and COOH.

The hydrodynamic size of the carbon dots was found to be 135.9 nm ± 3.7 nm and 130 nm ± 3 nm for BR-CDots and BV-CDots respectively **(Figure 2A)**. The hydrodynamic sizes of the particles are higher than the anhydrous particle sizes that are apparent in TEM images **(Figure S1)** due to the presence of a solvation layer when nanoparticles are suspended in liquid.[50,51] UV-visible absorbance spectra of the BR-CDots and BV-CDots **(Figure 2B)** reveal absorbance properties that are typical of carbon dots.[2,52] The BR-CDots have higher absorbance than the BV-CDots in the range of 300 nm to 500 nm, with their absorbance behaviors becoming more similar at higher wavelengths. Fluorescence spectra collected for the carbon dots illustrate that for since biliverdin and bilirubin respectively respond to biliverdin reductase and bilirubin oxidase, carbon dots synthesized from these precursors may respond to these enzymes. Particle size was measured with nanoparticle tracking analysis over a period of 10 days **(Figure 2D)**. The results reveal that the nanoparticles exhibit a reduction in size as a result of enzyme treatment, indicating potential degradation of the nanoparticles in response to enzymes. This is potentially favorable for long-term experiments where *in vitro* or *in vivo* biodegradability may be desirable.

The pH responsiveness of the particles was evaluated through the collection of absorbance and fluorescence spectra at pH values

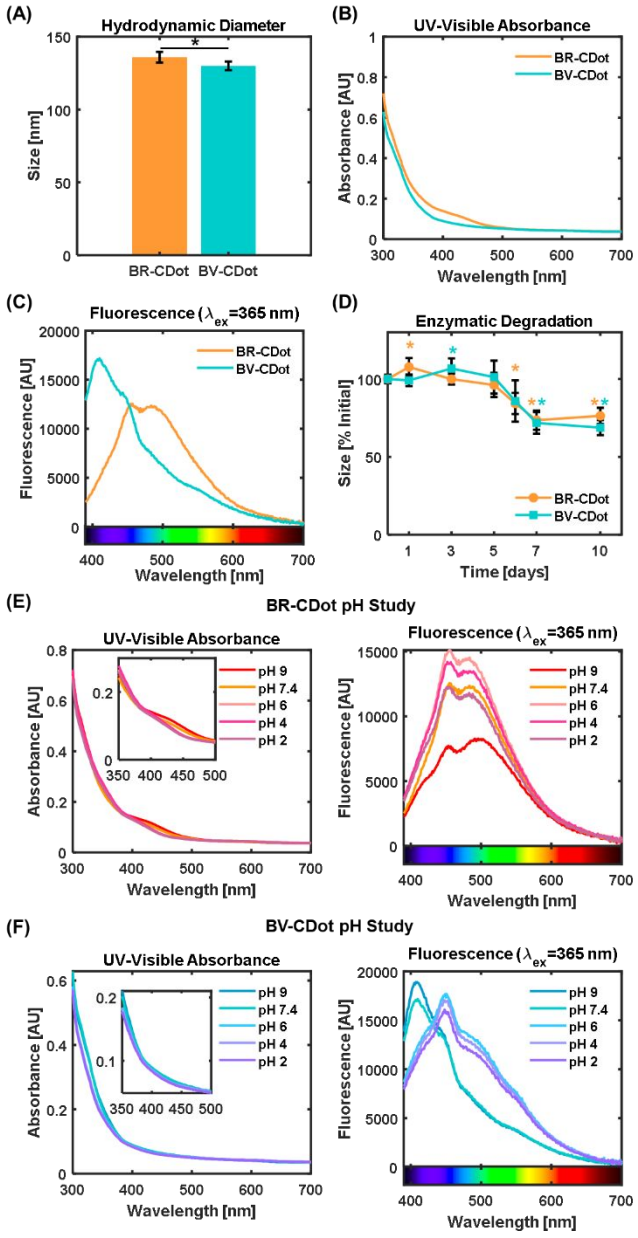

Figure 2. Photophysical properties and stimuli-responsive behavior. **(A)** Hydrodynamic size determined by nanoparticle tracking analysis. * indicates statistical significance (P<0.05). Error bars represent standard deviation across three to twelve runs (the number of usable runs was automatically determined by the software). **(B)** Absorbance spectroscopy of BR-CDots and BV-CDots at a pH of 7.4. **(C)** Fluorescence spectroscopy of CDots for an excitation wavelength of 365 nm and gain of 100 at a pH of 7.4. BR-CDots have a red-shifted fluorescence emission compared to that of BV-CDots. **(D)** Enzymatic degradation of BR-CDots and BV-CDots. BR-CDots were exposed to bilirubin oxidase and BV-CDots were exposed to biliverdin reductase. Size is presented as a percentage of the initial hydrodynamic size. Asterisks represent statistical significance (P<0.05) with respect to the initial size. An overall reduction of particle size as a result of enzyme treatment is observed. **(E)** Effect of pH on BR-CDot absorbance and fluorescence behaviour. Minor changes in absorbance behavior and more dramatic changes to fluorescence intensity are observed with changes in pH. Spectra depict representative data from two trials. **(F)** Effect of pH on BV-CDot absorbance and fluorescence behaviour. Changes to fluorescence intensity and fluorescence emission peak are observed with changes in pH. Spectra depict representative data from two trials.

ranging from a pH of 2 to a pH of 9. For the BR-CDots, some changes in absorbance behavior in the range of 350 nm to 500 nm are observed, with a slight decrease in absorbance for lower pH values. The fluorescence intensity of the BR-CDots was also altered by pH. A high pH of 9 led to the lowest fluorescence intensity, while lower pH values of 7.4 and 6 each led to increases in fluorescence intensity. A further reduction of pH values to 4 and 2 led to a reduction of fluorescence intensity. This indicates a non-linear dependence of fluorescence intensity on pH. However, a direct relationship between fluorescence intensity and pH is apparent for a pH range of 2 to 6 and a pH range of 6 to 9. The effects of cell health on intracellular pH and extracellular pH have been extensively studied.[53] Thus, the BR-CDots may serve as a fluorometric pH sensor for specific pH ranges, for example to distinguish between normal cell pH (intracellular pH ≈ 7.2, extracellular pH ≈ 7.4) and cancer cell pH (intracellular pH > 7.2, extracellular pH ≈ 6.7–7.1).[54,55] Interestingly, the BR-CDot fluorescence spectra have a dominant peak and a less prominent peak. For example, for pH 9 there is a smaller peak at ≈ 450 nm and a slightly higher peak at ≈ 490 nm. The intensities of the two peaks become approximately equal at a pH of 7.4, after which the lower-wavelength peak becomes more prominent for lower pH values. The ratio between the intensities of the two peaks is a potential parameter that can be used to distinguish between high and low pH values.

For the BV-CDots, pH altered both the fluorescence intensity and the wavelength of peak fluorescence. For a pH of 9 and a pH of 7.4, the fluorescence peak occurred at ≈ 410 nm, with a lower fluorescence intensity for a pH of 7.4 compared to a pH of 9. When the pH is lowered to 6, there is a red-shifting of the fluorescent peak to ≈ 450 nm. Fluorescence intensity then continues to decrease with a decrease in pH from a pH of 6 to a pH of 4 or 2. Thus, for the BV-CDots, the fluorescence intensity in conjunction with the wavelength of peak fluorescence can be used to evaluation pH.

To evaluate long-term particle stability at various pH values, we collected fluorescence spectra from pH-adjusted particles incubated at physiological temperature (37 °C) over a span of eight days. BR-CDots and BV-CDots each had stable fluorescence for at least 2 days at all tested pH levels **(Figure S3, Figure S4)**. BR-CDots in particular had high stability at a pH of 7.4 (stable for 8 days) and at a pH of 9, 4, and 2 (stable for at least 6 days). BV-CDots were stable for 2 days at a pH of 7.4 and pH of 9, and for over 6 days at pH 6, 4, and 2. These results demonstrate favorable short-term stability of the BR-CDot and BV-CDot fluorescence properties, with long-term stability at some pH levels.

Due to bilirubin's known NIR fluorescence emission [39], we further evaluated BR-CDot fluorescence behavior for higher excitation wavelengths. BR-CDots had high fluorescence emission intensities for excitation wavelengths of 465, 565, and 600 nm, with emissions in the NIR region **(Figure S5)**. We also conducted fluorescence microscopy on drop-casted solutions to compare the imageability of BR-CDots with methylene blue **(Figure S6)**, a commercially available dye commonly used for near-infrared fluorescence imaging.[56,57] These experiments revealed that BR-CDots have comparable or greater fluorescence intensity than methylene blue when imaged with Tetramethylrhodamine (TRITC) and cyanine 5 (Cy5) filter. Taking into consideration the stimuli-responsive behavior of these carbon dots, as well as the potential for carbon dot surface functionalization

for targeted imaging, BR-CDots can provide some advantages over the use of traditionally-used commercially-available dyes.

Particle biocompatibility and near-infrared tissue imaging

Biocompatibility is an important consideration in the evaluation of imageable nanoparticles. To examine the biocompatibility of these particles, 3-(4,5dimethylthiazol-2-yl)-2,5-diphenyltetrazolium bromide (MTT) assays were conducted with MCF-7, MDA-MB-231, and Hep G2 cells **(Figure 3A)**. These cell lines are metastatic breast cancer cells, triple-negative breast cancer cells, and liver cancer cells, respectively. All three cell lines exhibited high metabolic activity (>75%) when exposed to low concentrations of BR-CDots or BV-CDots. In fact, low concentrations of BR-CDots in some cases increased metabolic activity to higher than that of the control cells, while higher concentrations returned metabolic activity to normal levels. Due to pure bilirubin's poor solubility in water, comparisons between the metabolic activity of bilirubin-treated cells and BR-CDot-treated cells is not possible. High concentrations of BV-CDots decreased metabolic activity of the cells. However, this may have been due to increased uptake of BV-CDots as a result of their smaller size, as size has been found to play a role in nanoparticle uptake within cells.[58]

Due to the favorable biocompatibility and fluorescence behavior of BR-CDots, we further evaluated their potential for use as a near-infrared imaging contrast agent in biological tissue using excitation wavelengths above 600 nm. BR-CDots were injected just beneath the surface of chicken breast tissue, and imaged using a Spectrum In Vivo Imaging System (IVIS). Additional images were taken with another layer of chicken placed on top of the injection site, providing a depth of 8.5 mm for the BR-CDot fluorescence to penetrate **(Figure 3B)**. BR-CDots provided notable fluorescence contrast for a variety of excitation and near-infrared emission wavelengths, with representative images for excitation wavelengths of 605, 640, and 675 nm and emission at 840 nm shown in **Figure 3B i**. Images for other excitation and emission pairs are provided in **Figure S7-S16**. Despite a loss of signal with increased tissue depth, the location of BR-CDots is still apparent **(Figure 3B i)**. Region of interest (ROI) analysis of images **(Figure 3B ii)** confirm that BR-CDots provide a high radiant efficiency over a range of excitation and emission wavelengths. ROI quantification for lower wavelengths is presented in **Figure S17**. For excitation wavelengths of 605 nm, 640 nm, and 675 nm, the level of signal penetration at 8.5 mm as a percentage of the signal at the surface level is provided in **Figure S18**. This data illustrates that a higher percentage of the surface-level signal is transmitted at higher emission wavelengths. This suggests a reduction of signal transmission for lower emission wavelengths, which is in line with what is expected due to interference caused by biological tissue. This further confirms the importance of imaging in the near-infrared emission window.

To further evaluate the potential utility of BR-CDots for use in biological imaging, experiments were conducted in which BR-CDots were injected subcutaneously in the rear leg of a euthanized mouse. IVIS images obtained of the mouse under 605 nm excitation illustrate high radiant efficiency at the location of nanoparticle injection **(Figure 3C)**. This excitation wavelength was chosen because tissue phantom imaging experiments revealed that the BR-CDots had a higher average radiant efficiency for 605 nm excitation than for excitation wavelengths of 640 nm or 675 nm. This is likely due to decreasing BR-CDot absorbance with increasing wavelength. ROI analysis of the injection site demonstrated the ability of these particles to provide strong near-infrared fluorescence emission within biological tissues, with strong emission in the range of 660 nm to 840 nm.

Conclusions

We have demonstrated that carbon dots derived from endogenous bile pigments bilirubin and biliverdin are stimuli-responsive. BR-CDots exhibited changes in fluorescence intensity in response to changes in pH. BV-CDots exhibited changes in both fluorescence intensity and fluorescence peak emission wavelength in response to changes in pH. When BR-CDots were exposed to bilirubin oxidase and BV-CDots were exposed to biliverdin reductase, they exhibited decreases in hydrodynamic particle size, indicating potential degradation. BR-CDots exhibited high NIR fluorescence emission for higher excitation wavelengths, and provided high radiant efficiency and strong contrast in *ex vivo* chicken tissue phantom imaging and *ex vivo* imaging in mice. Those properties can be further explored in the future using *in vivo* biodistribution studies. This work is the first demonstration of rational selection of endogenous tetrapyrrolic stimuli-responsive carbon dot precursors which lead to stimuli-responsive pH sensing and enzymatic degradation. This sets the foundation for the use of carbon nanoparticles synthesized from endogenous precursors to generate an inherently stimuli-responsive system with strong NIR fluorescence emission without the need for post-synthesis surface modification.

In recent years, research in carbon dots has grown rapidly and a variety of carbohydrate precursors have been used for synthesizing these particles. Careful screening of precursors to design particles with special properties is important. This work highlights that precursors are a key determinant of carbon dot performance. Importantly, the use of stimuli-responsive precursors could produce stimuli-responsive nanoparticles that have a variety of biomedical applications. For example, BR-CDots and BV-CDots have potential applications in cellular pH imaging, especially because the pH of cancer cells differs from that of healthy cells. BR-CDots in particular can be surface-functionalized with targeted peptides, antibodies, or other ligands to enable targeted imaging in the near-infrared window. The use of nanoparticles for pH sensing and bioimaging has been extensively explored and can provide many advantages over traditional dye-based methods.[59–69] However, the goal of this work was to draw attention to the stimuli-responsive properties that can be imparted upon carbon dots through the use of stimuli-responsive precursors.

Experimental Section

Disclaimer

Certain commercial materials are identified in this paper to specify the experimental procedure adequately. Such identification is not intended to imply recommendation or endorsement by the National

Institute of Standards and Technology, nor is it intended to imply that the materials or equipment identified are necessarily the best available for the purpose.

Materials

Bilirubin and biliverdin hydrochloride were purchased from Frontier Scientific. Bilirubin Oxidase from Myrothecium Verrucaria, Biliverdin Reductase A Human, and NADPH disodium salt were purchased from Sigma Aldrich. Bilirubin oxidase was dissolved in water at a final concentration of 0.5 units/μL. Normocin was purchased from InvivoGen, and MTT was purchased from Biosynth.

Carbon Dot Synthesis

Bilirubin and biliverdin hydrochloride were each separately dissolved overnight at a concentration of 100 mg/mL in a solution of 500 μL water /500 μL DMSO. Each solution was placed in a separate, clean 50-mL PTFE-lined autoclave vessel. Samples were placed in the oven at 162.5 °C for 8 h, after which they were allowed to cool overnight. The following day, samples were removed from the vessels, and any excess liquid was removed through rotovapping and lyophilization. Dried samples were dissolved in 5 mL of water, and probe sonicated on a Qsonica Q700 probe sonicator for 30 min with an amplitude of 1, on time of 1 s, and off time of 2 s. Samples were then filtered using syringe filters with a pore size of 0.22 μm, lyophilized, and resuspended at a concentration of 1 mg/mL in water.

Nanoparticle Sizing and Enzymatic Degradation

BR-CDot. 1 milliliter of BR-CDot solution was placed in a capped 4-mL glass scintillation vial. 10 microliters to 25 microliters of 1 mol/L NaOH solution was added to increase the CDot solution pH to 8~9. Bilirubin oxidase solution (2 μL) was added to the CDot solution. Samples were shielded from light using foil, and were placed on a stir plate at 52.4 rad/s (500 rpm) and 40 °C. Particle size was measured

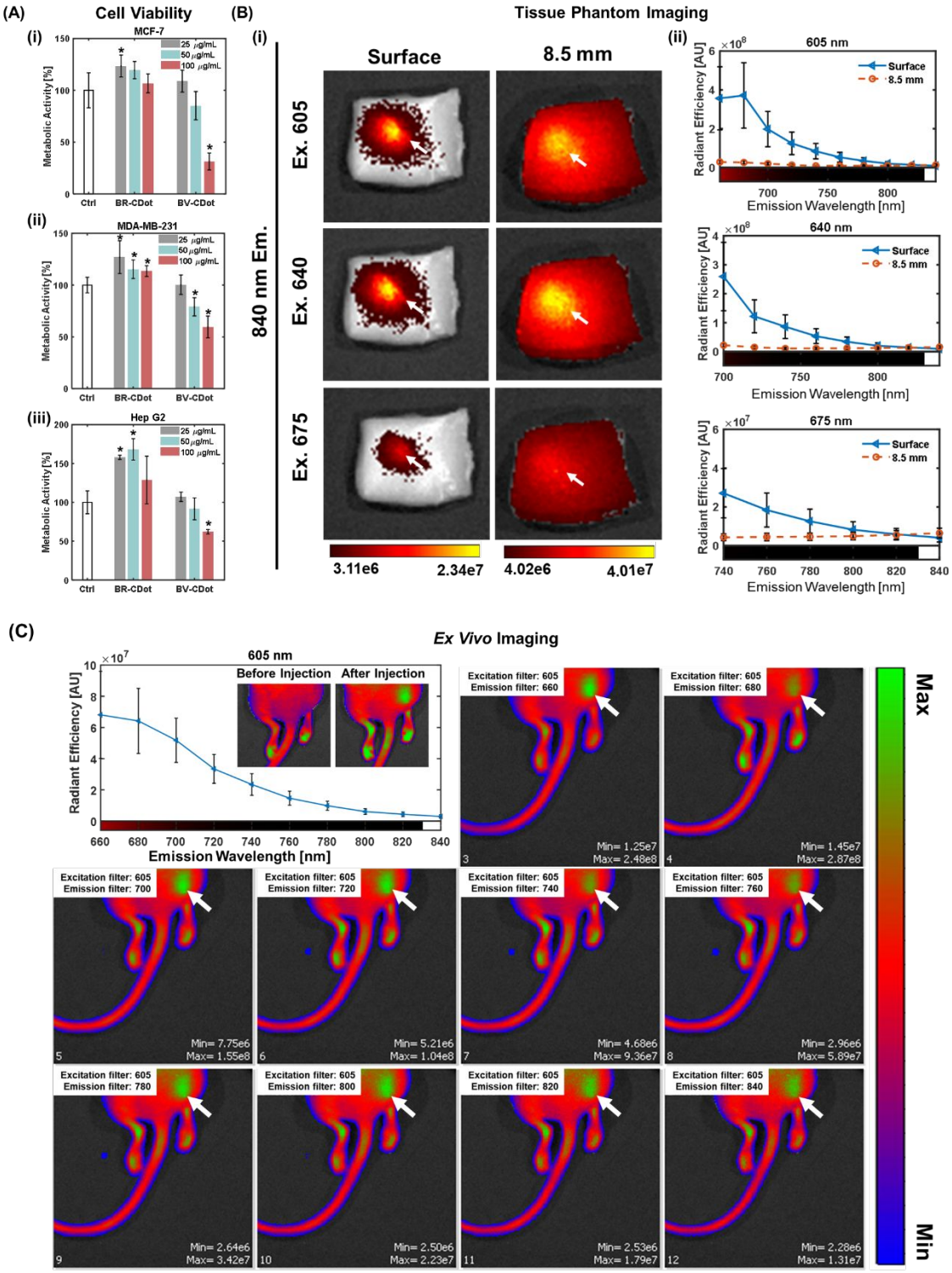

Figure 3. Biocompatibility and BR-CDot Near-infrared Imaging. **(A)** Metabolic activity of cells exposed to various concentrations of BR-CDots and BV-CDots. Particle concentrations are expressed in μg/mL. **(i)** Metabolic activity of MCF-7 breast cancer cells. **(ii)** Metabolic activity of MDA-MB-231 triple-negative breast cancer cells. **(iii)** Metabolic activity of Hep G2 liver cancer cells. Error bars represent standard deviation. * represents statistical significance from control, with $P<0.05$. BR-CDots lead to high metabolic activity in all cell lines. High concentrations of BV-CDots lead to decreased metabolic activity in all cell lines. **(B)** *Ex vivo* fluorescence imaging of BR-CDots injected in a chicken breast tissue phantom. **(i)** Images are presented for excitation wavelengths of 605 nm, 640 nm, and 675 nm, with emission measured at 840 nm. BR-CDots provide high signal in the near-infrared region, even under 8.5 mm of chicken tissue. White arrows indicate location of nanoparticles. **(ii)** Background-subtracted radiant efficiency of BR-CDots for excitation wavelengths of 605 nm, 640 nm, and 675 nm. ROI background subtraction was conducted as described in the methods. **(C)** *Ex vivo* imaging of mouse injected with BR-CDots. Images were acquired for an excitation wavelength of 605 nm. White arrows indicate the location of nanoparticles. ROI analysis displays strong radiant efficiency in the near-infrared region. Calculated ROIs were background-subtracted as described in the methods.

using a ParticleMetrix Zetaview system before enzyme exposure, and at 1, 3, 5, 6, 7, and 10 days after enzyme exposure was initiated. Average nanoparticle size was calculated for each of three to twelve runs using the ParticleMetrix software, and the averages and standard deviations across the runs were then calculated.

BV-CDot. 1 milliliter of BV-CDot solution was placed in a capped 4-mL glass scintillation vial. 10 microliters to 25 microliters of 1 mol/L NaOH solution was added to increase the CDot solution pH to 8∼9. NADPH (15.9 mg), a cofactor for biliverdin reductase, was added to the BV-CDot solution and allowed to mix for 10 min to 15 min, after which 2 μL biliverdin reductase was added. Samples were shielded from light using foil, and were placed on a stir plate at 52.4 rad/s (500 rpm) and 40 °C. Particle size was measured using a ParticleMetrix Zetaview system before enzyme exposure, and at 1, 3, 5, 6, 7, and 10 days after enzyme exposure was initiated. Average nanoparticle size was calculated for each of three to twelve runs using the ParticleMetrix software, and the averages and standard deviations across the runs were then calculated.

UV-Visible Spectroscopy

UV-visible spectra were collected for wavelengths ranging from 350 nm to 900 nm using a Thermo Scientific Genesys 10S UV−Vis spectrophotometer. CDot samples were not diluted for absorbance measurements. The baseline measurement was taken using 1 mL of water.

Transmission Electron Microscopy (TEM)

Microscopy samples were prepared on 300 to 400-mesh carbon-coated copper TEM grids. Undiluted CDot samples (2-20 μL) were drop-cast onto each TEM grid and allowed to settle for 2-10 min, after which the excess liquid was wicked away with qualitative filter paper. Samples were then placed within centrifuge tubes and stored dry until the imaging session. TEM images were acquired with an acceleration voltage of 80 keV on a FEI tecnai T12 TEM instrument. High-resolution TEM images were acquired at 200 keV on a JEOL Cryo 2100 TEM.

Quantification of d-spacing. Lattice fringe d-spacing was computed using ImageJ. A global scale was assigned for the image using the scale bar embedded within the image. A line was drawn perpendicular to the lattice fringes of interest. The intensity profile of the line was determined using the "Plot profile" tool, with a higher intensity corresponding to the brighter portions of the image. The distance between adjacent peaks (representing high intensity locations within the image) were computed and averaged.

Fluorescence Spectroscopy

Fluorescence spectra were acquired for undiluted 100 μL samples of each particle type. Excitation wavelengths of 365 nm, 465 nm, 565 nm, and 600 nm were used, with gains of 100, 100, 150, and 175 respectively. Fluorescence spectra were collected on a TECAN infinite M200PRO or a Biotek Synergy Neo2Microplate reader.

pH Responsiveness/Stability Studies

1 milliliter of BR-CDot or BV-CDot solution was placed in five separate 5 mL glass scintillation vials. The pH of the solution was adjusted either by the addition of 1 mol/L solution of HCl or NaOH to pH ~2, 4, 6, 7.4 and 9. The pH of the solution of each vial was constantly monitored by a HALO® Wireless pH Meter attached with microbulb. The change in fluorescence was recorded by taking 100 μL solution from each of the vials at the definite time interval.

Fluorescence Microscopy on Drop-Casted Samples

Methylene blue was dissolved in water at a concentration of 1 mg/mL. 20 μL of samples were dropcasted onto glass slides and covered with a cover slip. The slides were air dried before being imaged under a Nikon Ti2-E Inverted Automated Research Microscope with a 20X objective. A Pco.edge 4.2bi back illuminated cooled sCMOS camera was used for bright field imaging, and DAPI/GFP/TRITC/Cy5 fluorescent channels were used for imaging purposes. Integrated fluorescence intensity was analyzed in ImageJ using the "Integrated Density" measurement.

Fourier Transform Infrared Spectroscopy

FT-IR samples were prepared by dropping the nanoparticle solution onto Kevley MirrIR corner frosted FT-IR slides, after which they were placed under vacuum until they had completely dried. FT-IR measurements were taken using a Thermo Nicolet Nexus 670 FT-IR with the smart refractor accessory.

X-ray Photoelectron Spectroscopy

Gold-coated silicon wafer sample substrates were cleaned with piranha cleaning solution. 5 microliters of each sample were placed on the cleaned gold-coated silicon substrate and allowed to dry under vacuum, after which another 5 μL of each sample were deposited and allowed to dry again under vacuum. XPS measurements were performed on a Kratos Analytical Axis Ultra DLD instrument with a monochromated Al Kα X-ray source at 150 W (10 mA, 15 kV). X-rays were collected at a 0° angle from surface normal on an area of 300 μm × 700 μm. Low resolution survey scans (160 eV pass energy, 0.5 eV step size) and high resolution narrow scans (40 eV pass energy, 0.1 eV step size) of O 1s, N 1s, C 1s, and S 2p were obtained. Charge neutralization was used during measurements. The binding energy scale was calibrated to the C1s, C*- C aliphatic carbon peak at 284.5 eV. The CasaXPS program was utilized to analyze the spectra.

MTT Assays

3-(4,5dimethylthiazol-2-yl)-2,5-diphenyltetrazolium bromide (MTT) was dissolved at a concentration of 5 mg/mL in phosphate buffered saline (PBS). Cells were grown to 70 % to 80 % confluence in 25 cm^2 tissue culture flasks. Dulbecco's modified eagle medium (DMEM) supplemented with 10 % fetal bovine serum (FBS), 1 % Penicillin-Streptomycin solution, and 100 μg/mL Normocin was utilized for culture of all three cell lines (MCF-7, MDA-MB-231, and HepG2). Cells were plated at a concentration of 10,000 cells/well in 96-well plates and were incubated overnight under 37 °C under standard cell culture conditions. CDot solutions (1 mg/mL starting concentration) were diluted to concentrations of 100 μg/mL, 50 μg/mL, or 25 μg/mL in medium, and 100 μL of CDot-containing medium was added to each well. The cells were incubated for 24 h at 37 °C under standard cell culture conditions. The medium from each well was then

discarded and replaced with 100 µL diluted MTT solution (15 µL MTT solution in PBS, 85 µL completed medium) and cells were incubated for a further 4 h. Afterwards, the medium from each well was discarded, and formazan crystals in each well were dissolved with 100 µL DMSO. The 650 nm and 570 nm absorbance of each well was measured, and viability was calculated by:

$$\%\ Viability = \left(\frac{Sample\ Abs_{570} - Sample\ Abs_{650}}{Control\ Abs_{570} - Control\ Abs_{650}}\right) * 100\%$$

(Equation 2)

Four or more wells were used for each condition, and results were reported as an average, with error bars representing standard deviation.

Tissue Phantom Imaging

Fresh chicken breasts were purchased from a grocery store. 100 microliters BR-CDots were injected directly beneath the surface of a chicken tissue sample. Fluorescence images were acquired on an IVIS imaging system for excitation wavelengths of 465 nm, 500 nm, 605 nm, 640 nm, and 675 nm. For images collected at an 8.5-mm depth, a second chicken tissue sample was placed on top chicken tissue into which BR-CDots were placed, and images were subsequently retaken.

***Ex Vivo* Mouse Imaging**

The experimental protocol was approved by the Institutional Animal Care and Use Committee (IACUC), University of Illinois, Urbana−Champaign, and satisfied all University and National Institutes of Health (NIH) rules for the humane use of laboratory animals. 100 microliters BR-CDots were injected subcutaneously in the right rear leg of a previously euthanized athymic mouse. IVIS images were acquired with an excitation wavelength of 605 nm.

ROI analysis

For each sample, one ROI measurement was taken at the nanoparticle injection site, and one ROI measurement was taken at a location not containing nanoparticles. The second ROI measurement was subtracted from the first, providing a measurement of the net average radiant efficiency. Sample ROIs for tissue phantom imaging and *ex vivo* mouse imaging are provided in **Figure S19** and **Figure S20** respectively.

Author Contributions

Conceptualization (PF, DP)
Investigation (PF, MM, PM)
Visualization (PF, MBE, DP)
Supervision (DP)
Writing – original draft (PF)
Writing – review & editing (PF, MBE, DP)

Conflicts of interest

Prof Pan is the founder or co-founder of three university-based start-ups. None of these entities, however, supported this work.

Acknowledgements

This work was carried out in part in the Frederick Seitz Materials Research Laboratory Central Research Facilities, University of Illinois. We gratefully acknowledge the Chemical and Bio-molecular Engineering department shared facilities for access to their fluorescence spectrometer. This project was funded through grants from the National Institutes of Health, Department of Defense, and University of Illinois. P. Fathi was supported by the National Physical Science Consortium and the National Institute of Standards & Technology through an NPSC graduate fellowship, and by the Nadine Barrie Smith Memorial Fellowship from the Beckman Institute. Research reported in this publication was supported by the National Institute of Biomedical Imaging and Bioengineering of the National Institutes of Health under Award Number T32EB019944. We gratefully acknowledge Kristen Steffens for collection and analysis of XPS spectra, and Ramya Vishnubhotla for preparation of the gold-coated silicon substrate. The authors wish to acknowledge the helpful comments of the reviewers, which enabled us to better understand the stimuli-responsive behaviors of the BR-CDots and BV-CDots.

References

1 S. Zhu, R. Tian, A. L. Antaris, X. Chen and H. Dai, *Adv. Mater.*, 2019, **31**, 1–25.
2 P. Fathi, J. S. Khamo, X. Huang, I. Srivastava, M. B. Esch, K. Zhang and D. Pan, *Carbon N. Y.*, 2019, **145**, 572–585.
3 Z. L. Wu, M. X. Gao, T. T. Wang, X. Y. Wan, L. L. Zheng and C. Z. Huang, *Nanoscale*, 2014, **6**, 3868–3874.
4 Y. Dong, H. Pang, H. Bin Yang, C. Guo, J. Shao, Y. Chi, C. M. Li and T. Yu, *Angew. Chemie - Int. Ed.*, 2013, **52**, 7800–7804.
5 X. Bao, Y. Yuan, J. Chen, B. Zhang, D. Li, D. Zhou, P. Jing, G. Xu, Y. Wang, K. Holá, D. Shen, C. Wu, L. Song, C. Liu, R. Zbořil and S. Qu, *Light Sci. Appl.*, 2018, **7**, 1–11.
6 H. Li, X. He, Y. Liu, H. Huang, S. Lian, S. T. Lee and Z. Kang, *Carbon N. Y.*, 2011, **49**, 605–609.
7 D. Li, P. Jing, L. Sun, Y. An, X. Shan, X. Lu, D. Zhou, D. Han, D. Shen, Y. Zhai, S. Qu, R. Zbořil and A. L. Rogach, *Adv. Mater.*, 2018, **30**, 1–8.
8 L. Li, R. Zhang, C. Lu, J. Sun, L. Wang, B. Qu, T. Li, Y. Liu and S. Li, *J. Mater. Chem. B*, 2017, **5**, 7328–7334.
9 I. Srivastava, S. K. Misra, I. Tripathi and A. Schwartz-duval, *Adv. Biosyst.*, 2018, **1800009**, 1–11.
10 I. Srivastava, J. S. Khamo, S. Pandit, P. Fathi, X. Huang, A. Cao, R. T. Haasch, S. Nie, K. Zhang and D. Pan, *Adv. Funct. Mater.*, 2019, **1902466**, 1902466.
11 S. K. Misra, I. Srivastava, I. Tripathi, E. Daza, F. Ostadhossein and D. Pan, *J. Am. Chem. Soc.*, 2017, **139**, 1746–1749.
12 Y. P. Sun, B. Zhou, Y. Lin, W. Wang, K. A. S. Fernando, P. Pathak, M. J. Meziani, B. A. Harruff, X. Wang, H. Wang, P. G. Luo, H. Yang, M. E. Kose, B. Chen, L. M. Veca and S. Y. Xie, *J. Am. Chem. Soc.*, 2006, **128**, 7756–7757.
13 K. M. Chan, W. Xu, H. Kwon, A. M. Kietrys and E. T. Kool, *J. Am. Chem. Soc.*, 2017, **139**, 13147–13155.
14 H. Wu, Y. Chen, X. Dai, P. Li, J. F. Stoddart and Y. Liu, *J. Am. Chem. Soc.*, 2019, **141**, 6583–6591.

15 D. H. Shin, J. S. Lee, J. Jun, S. G. Kim and J. Jang, *ACS Appl. Mater. Interfaces*, 2015, **7**, 1746–1751.
16 P. Yang, Y. Tian, Y. Men, R. Guo, H. Peng, Q. Jiang and W. Yang, *ACS Appl. Mater. Interfaces*, 2018, **10**, 42039–42049.
17 H. Ali, S. K. Bhunia, C. Dalal and N. R. Jana, *ACS Appl. Mater. Interfaces*, 2016, **8**, 9305–9313.
18 L. Zhou, X. Qu, D. Zheng, H. Tang, D. Liu, D. Qu, Z. Xie, J. Li and D. Qu, *ACS Appl. Mater. Interfaces*, 2017, **9**, 41332–41338.
19 Y. Wen, Q. Jia, F. Nan, X. Zheng, W. Liu, J. Wu, H. Ren, J. Ge and P. Wang, *Chem. - An Asian J.*, 2019, **14**, 2162–2168.
20 F. Wu, H. Su, K. Wang, W. K. Wong and X. Zhu, *Int. J. Nanomedicine*, 2017, **12**, 7375–7391.
21 Y. Li, X. Zheng, X. Zhang, S. Liu, Q. Pei, M. Zheng and Z. Xie, *Adv. Healthc. Mater.*, 2017, **6**, 1–6.
22 F. Wu, H. Su, Y. Cai, W. K. Wong, W. Jiang and X. Zhu, *ACS Appl. Bio Mater.*, 2018, **1**, 110–117.
23 P. Fathi and D. Pan, *Nanomedicine*, , DOI:10.2217/nnm-2020-0125.
24 Y. Lee, H. Kim, S. Kang, J. Lee, J. Park and S. Jon, *Angew. Chemie - Int. Ed.*, 2016, **55**, 7460–7463.
25 Y. Lee, S. Lee, D. Y. Lee, B. Yu, W. Miao and S. Jon, *Angew. Chemie - Int. Ed.*, 2016, **55**, 10676–10680.
26 J. Y. Kim, D. Y. Lee, S. Kang, W. Miao, H. Kim, Y. Lee and S. Jon, *Biomaterials*, 2017, **133**, 1–10.
27 M. J. Kim, Y. Lee, S. Jon and D. Y. Lee, *Biomaterials*, 2017, **133**, 242–252.
28 D. E. Kim, Y. Lee, M. G. Kim, S. Lee, S. Jon and S. H. Lee, *Biomaterials*, 2017, **140**, 37–44.
29 D. Y. Lee, J. Y. Kim, Y. Lee, S. Lee, W. Miao, H. S. Kim, J. J. Min and S. Jon, *Angew. Chemie - Int. Ed.*, 2017, **56**, 13684–13688.
30 P. Fathi, H. J. Knox, D. Sar, I. Tripathi, S. K. Misra, F. Ostadhossein, M. B. Esch, J. Chan and D. Pan, *ACS Nano*, 2019, acsnano.9b01201.
31 T. Sakurai and K. Kataoka, *Chem. Rec.*, 2007, **7**, 220–229.
32 S. Murao and N. Tanaka, *Agric. Biol. Chem.*, 1981, **45**, 2383–2384.
33 J. D. Ostrow and R. V. Branham, *Gastroenterology*, 1970, **58**, 15–25.
34 J. W. Singleton and L. Laster, *J. Biol. Chem.*, 1966, **240**, 5518–5525.
35 P. Fathi, A. Roslend, K. Mehta, P. Moitra, K. Zhang and D. Pan, *Nanoscale*, , DOI:10.1039/d0nr08485a.
36 C. Alexander, G. G. Bellah and D. A. Lightner, *J. Am. Chem. Soc.*, 1975, **97**, 2579–2580.
37 A. A. Lamola, J. Eisinger, W. E. Blumberg, S. C. Patel and J. Flores, *Anal. Biochem.*, 1979, **100**, 25–42.
38 Y. F. Shen, M. R. Tsai, S. C. Chen, Y. S. Leung, C. T. Hsieh, Y. S. Chen, F. L. Huang, R. P. Obena, M. M. L. Zwulueta, H. Y. Huang, W. J. Lee, K. C. Tang, C. T. Kung, M. H. Chen, D. Bin Shieh, Y. J. Chen, T. M. Liu, P. T. Chou and C. K. Sun, *Anal. Chem.*, 2015, **87**, 7575–7582.
39 N. M. Htun, Y. C. Chen, B. Lim, T. Schiller, G. J. Maghzal, A. L. Huang, K. D. Elgass, J. Rivera, H. G. Schneider, B. R. Wood, R. Stocker and K. Peter, *Nat. Commun.*, 2017, **8**, 1–16.
40 S. Schutting, S. M. Borisov and I. Klimant, *Anal. Chem.*, 2013, **85**, 3271–3279.
41 D. Aigner, B. Ungerböck, T. Mayr, R. Saf, I. Klimant and S. M. Borisov, *J. Mater. Chem. C*, 2013, **1**, 5685–5693.
42 S. K. B. A. D. Souza and B. Suhail, *Int. Nano Lett.*, 2019, **9**, 203–212.
43 T. Guner, H. Yuce, D. Tascioglu, E. Simsek, U. Savaci, A. Genc, S. Turan and M. M. Demir, *Beilstein J. Nanotechnol.*, 2019, **10**, 2004–2013.
44 M. He, J. Zhang, H. Wang, Y. Kong, Y. Xiao and W. Xu, *Nanoscale Res. Lett.*
45 H. Liu, X. Zhao, F. Wang, Y. Wang, L. Guo, J. Mei and C. Tian, *Nanoscale Res. Lett.*, , DOI:10.1186/s11671-017-2137-2.
46 F. Fina, S. K. Callear, G. M. Carins and J. T. S. Irvine, *Chem. Mater.*, 2015, **27**, 2612–2618.
47 X. Wang, K. Maeda, A. Thomas, K. Takanabe, G. Xin, J. M. Carlsson, K. Domen and M. Antonietti, *Nat. Mater.*, 2008, **8**, 76–80.
48 J. Fevery, *Liver Int.*, 2008, **28**, 592–605.
49 R. Brodersen, *J. Biol. Chem.*, 1979, **254**, 2364–2369.
50 C. M. Maguire, M. Rösslein, P. Wick and A. Prina-Mello, *Sci. Technol. Adv. Mater.*, 2018, **19**, 732–745.
51 B. Demeler, T. L. Nguyen, G. E. Gorbet, V. Schirf, E. H. Brookes, P. Mulvaney, A. O. El-Ballouli, J. Pan, O. M. Bakr, A. K. Demeler, B. I. Hernandez Uribe, N. Bhattarai and R. L. Whetten, *Anal. Chem.*, 2014, **86**, 7688–7695.
52 B. De and N. Karak, *RSC Adv.*, 2013, **3**, 8286–8290.
53 G. Hao, Z. P. Xu and L. Li, *RSC Adv.*, 2018, **8**, 22182–22192.
54 B. A. Webb, M. Chimenti, M. P. Jacobson and D. L. Barber, *Nat. Rev. Cancer*, 2011, **11**, 671–677.
55 E. Persi, M. Duran-Frigola, M. Damaghi, W. R. Roush, P. Aloy, J. L. Cleveland, R. J. Gillies and E. Ruppin, *Nat. Commun.*, , DOI:10.1038/s41467-018-05261-x.
56 C. Zhang, D. Jiang, B. Huang, C. Wang, L. Zhao, X. Xie, Z. Zhang, K. Wang, J. Tian and Y. Luo, *Technol. Cancer Res. Treat.*, 2019, **18**, 1–9.
57 S. L. Hillary, S. Guillermet, N. J. Brown and S. P. Balasubramanian, *Langenbeck's Arch. Surg.*, 2018, **403**, 111–118.
58 E. Fröhlich, *Int. J. Nanomedicine*, 2012, **7**, 5577–5591.
59 F. Niu, Y. Xu, M. Liu, J. Sun, P. Guo and J. Liu, *Nanoscale*, 2016, **8**, 5470–5477.
60 Y. Liu, X. Zhi, W. Hou, F. Xia, J. Zhang, L. Li, Y. Hong, H. Yan, C. Peng, J. M. De La Fuentea, J. Song and D. Cui, *Nanoscale*, 2018, **10**, 19052–19063.
61 M. El-Hamadi and A. G. Schätzlein, *Fundam. Pharm. Nanosci.*, 2013, **6**, 543–566.
62 S. D. Hettiarachchi, E. Kirbas Cilingir, H. Maklouf, E. S. Seven, S. Paudyal, S. Vanni, R. M. Graham and R. M. Leblanc, *Nanoscale*, 2021, **13**, 5507–5518.
63 W. Liu, C. Li, Y. Ren, X. Sun, W. Pan, Y. Li, J. Wang and W. Wang, *J. Mater. Chem. B*, 2016, **4**, 5772–5788.
64 L. Xiao and H. Sun, *Nanoscale Horizons*, 2018, **3**, 565–597.
65 M. Chen, W. Wu, Y. Chen, Q. Pan, Y. Chen, Z. Zheng, Y. Zheng, L. Huang and S. Weng, *RSC Adv.*, 2018, **8**, 41432–41438.

66 C. Lu, Q. Su and X. Yang, *Nanoscale*, 2019, **11**, 16036–16042.
67 Q. Chen, X. Liu, J. Zeng, Z. Cheng and Z. Liu, *Biomaterials*, 2016, **98**, 23–30.
68 B. Korzeniowska, R. Nooney, D. Wencel and C. McDonagh, *Nanotechnology*, , DOI:10.1088/0957-4484/24/44/442002.
69 H. Lin, J. Su, R. K. Kankala, M. Zeng, S. F. Zhou and X. Lin, *Micromachines*, , DOI:10.3390/mi10090568.